

Nonlinear Formulation of the Bulk Surface Stress over Breaking Waves: Feedback Mechanisms from Air-flow Separation

James A. Mueller · Fabrice Veron

Received: 30 November 2007 / Accepted: 10 November 2008 / Published online: 28 November 2008
© Springer Science+Business Media B.V. 2008

Abstract Historically, our understanding of the air-sea surface stress has been derived from engineering studies of turbulent flows over flat solid surfaces, and more recently, over rigid complex geometries. Over the ocean however, the presence of a free, deformable, moving surface gives rise to a more complicated drag formulation. In fact, within the constant-stress turbulent atmospheric boundary layer over the ocean, the total air-sea stress not only includes the traditional turbulent and viscous components but also incorporates surface-wave effects such as wave growth or decay, air-flow separation, and surface separation in the form of sea-spray droplets. Because each individual stress component depends on and alters the sea state, a simple linear addition of all stress components is too simplistic. In this paper we present a model of the air-sea surface stress that incorporates air-flow separation and its effects on the other stress components, such as a reduction of the surface viscous stress in the separated region as suggested by recent measurements. Naturally, the inclusion of these effects leads to a non-linear stress formulation. This model, which uses a variable normalized dissipation rate of breaking waves and normalized length of the separation bubble, reproduces the observed features of the drag coefficient from low to high wind speeds despite extrapolating empirical wave spectra and breaking wave statistics beyond known limits. The model shows the saturation of the drag coefficient at high wind speeds for both field and laboratory fetches, suggesting that air-flow separation over ocean waves and its accompanying effects may play a significant role in the physics of the air-sea stress, at least at high wind speeds.

Keywords Air-flow separation · Breaking wind waves · Sea drag · Sea roughness · Wave boundary layer

J. A. Mueller (✉) · F. Veron
College of Marine and Earth Studies, University of Delaware, 112C Robinson Hall, Newark, DE 19716,
USA
e-mail: jmueller@udel.edu

F. Veron
e-mail: fveron@udel.edu

1 Introduction

Accurate evaluation and prediction of the stress at the surface of the ocean is critical to a large range of problems including air-sea heat, moisture, and gas exchanges, because turbulent diffusivity generally dominates its molecular counterpart by orders of magnitude, and thus, is the primary mechanism for transport. Unfortunately, the range of scales involved renders direct numerical simulation inadequate for models of these air-sea processes. Furthermore, high resolution data are sparse, and detailed experiments are unsuitable for routine field observations. Therefore, most applications require that the surface stress be derived from readily obtained and resolved variables. For flow over a smooth, flat plate, upon which boundary-layer turbulence theory is derived, this approach is quite successful because the stress in the vicinity of the surface can be considered to be constant, resulting in the well-known “law of the wall.” Succinctly, the law of the wall identifies three distinct layers: the viscous sublayer, where molecular stresses dominate, a log layer, where the turbulent stresses dominate, and a defect layer. Except in the defect layer, which is not considered further in this paper, the constant stress layer assumption leads to self-similar functions for the velocity profile in the form of the classical log-linear profiles. Unlike air flow over flat surfaces, individual stress components for the marine boundary layer are not well resolved, and their interactions are even more obscured. The complicating factor for the oceanic case is the presence of a free surface at the boundary. As the wind blows over the ocean, waves form, grow, interact with each other, and eventually break. In addition to the stress from the viscous boundary effects and turbulence, there is also stress due to the form of the waves (e.g. [Janssen 1989](#); [Belcher and Hunt 1993](#); [Makin et al. 1995](#); [Hare et al. 1997](#); [Edson and Fairall 1998](#)). Therefore, the stress at the surface is highly dependent on the sea state. For the purpose of this paper, we follow [Kudryavtsev and Makin \(2001\)](#) and split the stress from the waves (form drag) into the two main components: wave-induced and stress due to air-flow separation. For purely wind-wave seas, the wave-induced stress component is the momentum flux into the ocean, which creates, feeds, and maintains the waves. Air-flow separation stress occurs when the near-surface air is unable to follow the undulating surface locally because of extreme wave steepness, wave breaking or some other unresolved mechanism.

In recent years, several authors have used air-flow separation to explain both an increase and a decrease in the drag coefficient relative to extrapolated, bulk values at high wind speeds where data are sparse. On the one hand, field and laboratory data suggest that the drag coefficient peaks when the 10-m wind speed reaches roughly 34 m s^{-1} and afterwards decreases ([Powell et al. 2003](#); [Donelan et al. 2004](#)). On the other hand, previous numerical models of surface stress that include air-flow separation predict even higher values for the drag coefficient than those extrapolated from bulk parameterizations ([Kudryavtsev and Makin 2001](#); [Makin and Kudryavtsev 2002](#)). More recently, a first attempt, which explicitly models air-flow separation and its resulting feedback, has reproduced the near saturation of the drag coefficient at laboratory fetches ([Kudryavtsev and Makin 2007](#); hereafter KM07). The objective of our study is to formulate an explanation for the observed behaviour of the drag coefficient in the presence of air-flow separation for both laboratory and field fetches. Our model, which uses an empirical wave spectrum as well as a variable normalized dissipation rate of breaking waves and normalized length of the separation bubble, incorporates effects from air-flow separation yielding both a novel, non-linear formulation and different results from those previously reported.

2 The Atmospheric Boundary Layer

Using the bulk formulae, the turbulent momentum flux is expressed as:

$$-\overline{u'w'} = u_*^2 = \frac{\tau}{\rho_a} = C_D (U_{10} - U_0)^2, \tag{1}$$

where the primes indicate turbulent quantities (far from the influence of viscosity and waves) and the overbars represent ensemble averages. The air-side friction velocity and mean velocity are noted u_* and U , respectively; the density of air, ρ_a , is taken to be approximately 1.2 kg m^{-3} . The quantities C_D and τ are the bulk transfer coefficient for momentum, i.e. the drag coefficient, and the surface stress, respectively. Finally, a subscript 0 indicates the value taken at the interface and a subscript 10 indicates the 10-m height value. When the flow is neutrally buoyant, the velocity profile away from the boundary, where viscous effects are negligible, can then be evaluated from well-known law of the wall:

$$U(z) - U_0 = \frac{u_*}{\kappa} \ln \left(\frac{z + \delta}{z_0} \right) \tag{2}$$

where κ is the von Karman constant (≈ 0.4), z_0 is the roughness length, which parameterizes the influence of the roughness elements at the surface on the kinematics and dynamics of the flow, and $\delta = \alpha z_0$, usually with $\alpha = 1$, is introduced such that the profile is not singular at the surface ($z = 0$).

In smooth flow over a flat plate, a viscous sublayer forms near the surface in which the velocity profile is linear rather than logarithmic. In wall coordinates, $z^+ = zu_*/\nu$ and $U^+ = U/u_*$, the profile is also self-similar linear, $U^+ = z^+$. The van Driest damping function (van Driest 1956) approximates both the near-wall linear sublayer and the smooth transition to the log layer:

$$U^+ = A_1 \left(1 - \exp \left(\frac{-z^+}{A_1} \right) \right), \tag{3}$$

where A_1 is a constant, typically $O(10)$ for smooth flow (corresponding to the height of the viscous sublayer). The presence of waves causes the flow to depart from smooth flow and become transitionally rough for most wind speeds. Therefore, the moving, wavy bottom boundary needs to be considered.

3 Parameterization

3.1 Boundary Conditions and Profile

In the model presented here, once U_{10} is specified, the form for the velocity profile is determined using a hybrid of the van Driest damping function and the standard logarithmic profile described above. In fact, the profile is simply the summation of the two layers with the logarithmic layer exponentially damped in the near-wall region, as follows:

$$U(z) - U_0 = A_1 u_{*v} \left(1 - \exp \left(\frac{-z^+}{A_1} \right) \right) \frac{u_{*v}}{u_*} + \frac{u_*}{\kappa} \ln \left(\frac{z + \delta}{\delta} \right) \left(1 - \exp \left(\frac{-z^+}{A_1} \right) \right), \tag{4}$$

where $\rho_a u_{*v}^2$ represents the viscous component of the surface stress, and $A_1 = 10$ is the height of the viscous sublayer in wall coordinates. Finally, the surface drift follows [Wu \(1983\)](#) as:

$$U_0 = 15.2u_{*v}\sqrt{\frac{\rho_a}{\rho_w}} = 0.53u_{*v}, \tag{5}$$

where ρ_w is the density of the surface water. The profile given in [Eq. 4](#) offers a continuous (and second-order differentiable) formulation that smoothly connects the viscous and log layers. The modification of the van Driest component accounts for the roughness of the flow and converges to the standard definition given in [Eq. 3](#) for the smooth flow limit, i.e. the limit $z^+ \rightarrow 0$ yields $U^+ = z^+ u_{*v}^2 / u_*^2$, which reduces to $U^+ = z^+$ in the smooth flow limit where the surface stress is entirely due to viscosity. Accordingly, the viscous stress at the surface is $\nu dU/dz|_{z=0} = u_{*v}^2$, and outside the viscous sublayer, the profile converges to the standard form,

$$U(z) - U_0 = \frac{u_*}{\kappa} \ln\left(\frac{z + \alpha z_0}{z_0}\right), \tag{6}$$

with

$$\alpha = \exp\left(\frac{\kappa A_1 u_{*v}^2}{u_*^2}\right). \tag{7}$$

The coefficient, α , merely shifts the profile near the surface in order to match the linear sublayer such that at the limit $z^+ \rightarrow \infty$, the profile converges to:

$$U(z) - U_0 = \frac{u_*}{\kappa} \ln\left(\frac{z}{z_0}\right). \tag{8}$$

As the air flow tends toward the fully rough regime, the slope of the viscous sublayer velocity profile, in wall coordinates, decreases relative to the smooth case. Consequently, the viscous sublayer only plays a dominant role at low wind speeds, while the form drag dominates the stress for moderate to high wind speeds. The only remaining variables yet to be defined are the two friction velocities, u_* and u_{*v} , and their parameterization is the subject of the next section.

3.2 Surface Waves

In the present model, the bottom boundary is a surface wind-wave field of deep water, gravity and capillary wave modes. The wavenumber range is specified with an implicit lower limit, $k_{min} = 0.07^2 g / u_*^2$ ([Plant 1982](#)) where $g \approx 9.81 \text{ m s}^{-2}$ is the gravitational acceleration constant. The spectrum follows an empirical, directional wavenumber spectrum, $\Psi(k, \theta)$ ([Elfouhaily et al. 1997](#)), where k and θ are respectively the wavenumber and angle between the wind and wave propagation directions. This empirical wave spectrum captures the observed fetch dependent nature of both the high wavenumber ([Cox and Munk 1954](#); [Jähne and Riemer 1990](#); [Hara et al. 1994](#)) and low wavenumber ([Kitaigorodskii 1973](#); [Phillips 1985](#)) regimes. Therefore, the spectrum is not only a function of the friction velocity, u_* , but also the inverse wave age, Ω , which is a function of normalized fetch, $X^* = Xg / U_{10}^2$:

$$\Omega = U_{10}/c_p = 0.84 \tanh\left((X^*/X_0)^{0.4}\right)^{-0.75}, \tag{9}$$

where X is the fetch, c_p is the peak wave phase speed and $X_0 = 2.2 \times 10^4$ is an empirical constant ([Elfouhaily et al. 1997](#)).

3.3 Surface Stress and Air-flow Separation

Banner and Peirson (1998) found that the surface stress in the smooth flow limit is the upper limit for the tangential stress at the surface in the laboratory. Intuitively, and in the absence of contradicting data, this result seems reasonable for extension to field cases as a first approximation. In the model, the viscous surface stress without accounting for the effect of air-flow separation, $\tau_v^0 = \rho_a (u_{*v}^0)^2$, is approximated by the equivalent stress in the smooth flow limit. Here, the superscript 0 refers to values that do not consider the feedback effects of the air-flow separation. By prescribing the 10-m wind speed, profile form (Eq. 4), and roughness length for smooth flow, i.e. $z_0 = 0.11\nu/u_{*v}^0$, the equivalent stress for smooth flow can be found.

For the total stress at the surface in the presence of air-flow separation, the individual stress components (viscous, wave-induced, and separation) are converged upon and summed using:

$$\tau|_{z=0} = \rho_a u_*^2 = f_1 \tau_v^0 + f_2 \tau_w^0 + f_3 \tau_s^0, \tag{10}$$

where τ_w^0 and τ_s^0 are the surface wave-induced and separation stresses (without air-flow separation feedback effects), respectively. The parameters, f_1 , f_2 , and f_3 account for the effects of airflow separation on these stresses and will be discussed shortly. The wave-induced stress, τ_w^0 , is found by the integration of the contributions from all waves:

$$\tau_w^0|_{z=0} = \rho_w \int_{k_{min} - \frac{\pi}{2}}^{\infty} \int_{-\frac{\pi}{2}}^{\frac{\pi}{2}} \beta(k, \theta) \omega k \Psi(k, \theta) \cos \theta d\theta dk, \tag{11}$$

where $\beta(k, \theta)$ is the wave growth rate, and ω is the wave angular frequency. Except for the use of the hybrid velocity profile (Eq.4), the separation stress, τ_s^0 , is modelled as in Kudryavtsev and Makin (2001); their Eq. 14 with minor modification can be written as:

$$\tau_s^0|_{z=0} = \rho_a \varepsilon_b \gamma \int_0^{20\pi} \int_{-\pi}^{\pi} u_s(k)^2 \cos \theta \Lambda(k, \theta) d\theta dk, \tag{12}$$

where ε_b is the characteristic slope of the breaking wave, γ is an empirical constant relating the pressure fall due to the separation region to the velocity of the air flow, and finally $u_s(k) = U(\varepsilon_b/k) \cos \theta - c(k)$ is the wind speed at height $z = \varepsilon_b/k$, in reference to the wave phase speed $c(k)$. The upper wavenumber limit for contribution to the separation stress is taken to be 20π as in Makin and Kudryavtsev (2002). The effect of air-flow separation on each of these stress components must now be considered.

We assume that air-flow separation only occurs in the presence of a wave breaking event. Therefore, the occurrence of breaking waves is the foundation for the air-flow separation stress and feedback effects. The probability of a wave crest breaking within the wavenumber range $(\mathbf{k}, \mathbf{k} + d\mathbf{k})$ is:

$$P_{br}(k, \theta) = \frac{2\pi}{k} \tilde{L}, \tag{13}$$

where $\tilde{L} = \Lambda(k, \theta)kd\theta dk$ is the total length of breaking wave crests per unit area of ocean surface for waves within the wavenumber range $(\mathbf{k}, \mathbf{k} + d\mathbf{k})$. When the spectral

dissipation due to breaking is assumed to be roughly equal to the spectral wind energy input (Kudryavtsev and Makin 2001), \tilde{L} can be approximated as:

$$\Lambda(k, \theta)kd\theta dk = \frac{\beta(k, \theta)k^4\Psi(k, \theta)d\theta dk}{\omega b}, \tag{14}$$

where b is the normalized dissipation rate of breaking waves, often taken as a constant. Later, b will be shown to be dependent on the characteristic wave steepness and consequently a function of wavenumber.

For a monochromatic wave field, the fraction of sea surface area exposed to air-flow separation over a breaking wave would be:

$$\tilde{A} = LP_{br}, \tag{15}$$

where L is the length of the separation region normalized by the wavelength, i.e. the down-wind extent of the separation bubble as a fraction of the wavelength. Below, we discuss L in more detail. In the presence of multiple wave modes, some separated regions may overlap. For example, in the case where a large, dominant wave crest breaks and the separated region extends such that it covers a fraction of the surface containing subsequent smaller breaking waves, these smaller waves could not induce separation that would affect additional sea surface area. Therefore, noting that the fraction of area that is not affected by air-flow separation per unit wavenumber is $Q(k) = 1 - \int_{\theta} LP_{br}(k, \theta)$, the fraction of area per unit wavenumber exposed to separation is the fractional probability of unaffected area from all longer waves multiplied by the fraction of affected area of the corresponding monochromatic wave:

$$\tilde{A}(k) = \prod_{k' < k} [Q(k')] \times \int_{\theta} LP_{br}(k, \theta). \tag{16}$$

The total fraction of area exposed to air-flow separation is the area over all wavenumbers, i.e. $A = \int_k \tilde{A}(k)$. With the fraction of sea surface exposed to air-flow separation, the parameters f_1 , f_2 , and f_3 accounting for the effect of separation on the multiple stress components follow naturally:

$$f_1 = 1 - A, \tag{17}$$

$$f_2(k) = 1 - \int_0^k \tilde{A}(k'), \tag{18}$$

$$f_3(k) = \frac{\tilde{A}(k)}{\int_{\theta} P_{br}(k, \theta)}. \tag{19}$$

The first parameter f_1 simply accounts for the reduction of viscous stress due to the total sea surface area exposed to air-flow separation. Physically, this means that the viscous stress at the surface vanishes within the separation bubble, and is consistent with recent laboratory experiments (Reul 1998; Veron et al. 2007) that show the surface viscous stress is vastly reduced in the region of air-flow separation. The second parameter f_2 assumes that there is a cascade from all longer waves, represented as a cumulative sum of the fraction of sea surface area exposed to separation (Kudryavtsev and Makin 2007). Finally, the third parameter f_3 adjusts the separation stress from breaking wave statistics to the modified air-flow separation statistics. In other words, the probability of an air-flow separation event is less than or equal to that of a breaking wave event because multiple breaking waves could have overlapped separation regions. Accounting for feedback, the effective viscous, wave-induced, and

separation stresses respectively become $\tau_v = f_1 \tau_v^0$, $\tau_w = \int_k f_2 d\tau_w^0$, and $\tau_s = \int_k f_3 d\tau_s^0$, and the total stress is now:

$$\tau|_{z=0} = \tau_v + \tau_w + \tau_s, \tag{20}$$

where $d\tau_w^0$ and $d\tau_s^0$ are respectively the spectral densities of wave-induced and separation stresses without air-flow separation effects.

If the wave growth parameter is conceptualized as the rate of energy transferred from the wind to waves normalized by wave energy, then the presence of multiple wave modes intuitively affects the energy transfer. The dependence of the growth rate on the local turbulent stress within the inner layer stems from the theory of [Belcher and Hunt \(1993\)](#). Essentially, longer waves shelter shorter waves, resulting in reduced local turbulent stress for the inner region of shorter waves whose outer boundary is still within the inner region of the longer waves ([Makin and Kudryavtsev 1999](#)). Following [Belcher and Hunt \(1993\)](#); [Belcher \(1999\)](#); [Makin and Kudryavtsev \(1999\)](#) and [Hara and Belcher \(2002\)](#), we assume that the growth rate depends upon the local turbulent stress available for each wave mode, and the stress induced by each wave mode is constant within the inner region and zero outside of it. Approximating the wave-induced stress for each wave mode as a step function simplifies the parameterization considerably and does not seem to render drastically different drag coefficients compared to more complex decay functions ([Makin et al. 1995](#)). Therefore, within the constant stress layer, the wave-induced stress discontinuously becomes turbulent stress outside the wave boundary layer. We also assume that the separation stress from all wave modes is part of the turbulent stress throughout the constant-stress layer. Consequently, the maximum turbulent stress available for each wave mode is the summation of the total viscous and separation stresses and the wave-induced stress of all smaller waves. In other words, for each wave mode the stress carried by all shorter wave modes contributes to the stress in the wave growth parameter such that:

$$\beta(k, \theta) = \frac{C_b(k)\omega(k)}{\rho_a c(k)^2} \left(\tau_v + \tau_s + \int_k^\infty d\tau_w(k') \right) h(\theta), \tag{21}$$

where $C_b(k)$ is in the range 0.04 ± 0.02 ([Plant 1982](#)), $d\tau_w(k')$ is the spectral wave-induced stress and $h(\theta) = \cos^{2p}(\theta)$ is the directionality of the growth rate ([Phillips 1985](#)). The exponent, p , is implicitly given by the directionality of the wavenumber spectrum, assumed to be of the form $h(\theta)^{1/2}$, and generally $p \approx 1$ for the distant equilibrium range and $p > 1$ closer to the spectral peak. In practice, taking $p = 1$ for the entire range in the growth rate calculation does not change the results significantly because they are predominantly controlled by wind-wave angles close to zero. In other words, higher orders of p near the spectral peak do little to affect the results because these waves are already more closely aligned with the wind. To limit wave growth to the wind-wave regime, the following smooth cut-off for $C_b(k)$ is used:

$$C_b(k) = B - B \tanh\left(\frac{c(k)}{2u_*} - 1.8\pi\right), \tag{22}$$

where B is a constant taken to be 0.02. Thus, for young waves, the value for C_b is 0.04, which corresponds to Plant’s mean value. With increasing wave age, the constant changes smoothly to zero at the wind-wave limit and remains zero for all older waves, which in effect prohibits negative wave growth (i.e. the transfer of momentum from the waves beyond the wind-wave limit to the air).

Three of the empirically derived parameters used in modelling both the separation stress and resulting feedback, namely the breaking wave slope (ϵ_b), the normalized dissipation rate of the breaking wave (b), and the normalized length of the separation bubble (L), remain to be parameterized. The slope of breaking waves can be less than 0.2 on the low end (Wu and Yao 2004) and greater than 0.6 on the high end (Duncan 1981). For the dominant waves, the significant slope is often used as the characteristic breaking wave slope:

$$\epsilon = \frac{H_p k_p}{2} = \frac{4k_p}{2} \left[\int_{0.7f_p}^{1.3f_p} \Psi(f) df \right]^{\frac{1}{2}}, \tag{23}$$

where the subscript p denotes peak wave properties, f is the wave frequency, and H_p is the significant wave height of the peak waves. Here, we employ a slightly different, yet equivalent characteristic breaking slope as that above, and offer a unified form for the dominant and equilibrium regimes. Indeed, for the dominant waves, the significant slope scales (by a factor of 2) with the root-mean-square slope of the dominant waves. Thus, for both regimes, dominant and equilibrium, we can take the characteristic breaking wave slope as:

$$\epsilon_b(k) = 2 \left[\int S(k') dk' \right]^{\frac{1}{2}}, \tag{24}$$

where $S(k) = \int_{-\pi}^{\pi} k^2 \Psi(k, \theta) k d\theta$ is the slope spectrum. The limits of integration are found from a standard, logarithmic wavenumber bandwidth, which corresponds to the conversion of the wave frequency limits in the significant slope calculation (taken here as $0.5f_p$ and $1.5f_p$) to fractional wavenumber limits. Presumably, breaking wave events with small slopes are more likely to be a spilling wave, while the breaking events at greater slopes are more likely to be a plunging wave.

The normalized dissipation rate for breaking waves, b , has been found to span a wide range of values from 10^{-4} to 10^{-1} (e.g. Duncan 1981; Melville 1994; Phillips et al. 2001; Drazen 2006; Banner and Peirson 2007), and is thought to depend on the slope of breaking waves (Melville 1994). Indeed, recent work (Drazen 2006) suggests that the dependence of b on slope is split into the spilling and plunging regimes, respectively:

$$b = \Upsilon \epsilon_b^{\frac{1}{2}}, \tag{25}$$

$$b = \chi \epsilon_b^{\frac{5}{2}}. \tag{26}$$

Following Drazen et al. (2008), we take $\chi = 0.25$. Fitting the two regimes at the slope, 0.2, we find the value $\Upsilon = 0.01$, which is toward the lower end of the range, 0.007–0.019, suggested by the tabulated data from Duncan (1981).

Finally, we need to parameterize the fractional length, L , of the sea surface affected by air-flow separation. Earlier models proposed that $L = 0.75 \cos \theta$, where θ is the angle between the wind and wave propagation directions (Csanady 1985). Kudryavtsev and Makin (2007) assumed that the flow re-attached at the following crest, i.e. $L = 1$, in the case of co-propagating wind and waves. This certainly is the upper bound and, realistically, the length of the separated region is less than the wavelength. In both cases, the length of the air-flow separation region normalized by wavelength is a constant fraction of the wavelength. The length of the area exposed to the separation bubble, however, presumably depends upon the slope of the wave (Reul et al. 2008). Thus, we propose that

$$L(k) = \left(\varepsilon_b(k)^{\frac{1}{2}} + \frac{1}{4} \right) \cos \theta. \quad (27)$$

For the range of breaking slopes considered here, L ranges between 0.55 and 1 when the angle between the wave and wind directions is zero. We note, however, that the model results are not very sensitive to the choice of L and are qualitatively similar to the case when $L = 0.75 \cos \theta$ for all wave modes.

4 Results

We present here the model output for both laboratory and field fetches and compare the predictions with available data and parameterizations.

4.1 Laboratory Comparison

Experimental data at laboratory fetches offer insight not only into the behaviour of the drag coefficient at high wind speeds but also into the relative contributions of each stress component at lower wind speeds. This combination of data can be used to assess the role of air-flow separation in extreme conditions. Kunishi and Imasoto (see [Kondo 1975](#); [Garratt 1977](#)) performed a wind flume experiment at high wind speeds and found that the increase of the drag coefficient with wind speed lessened above $U_{10} = 27 \text{ m s}^{-1}$. Furthermore, their data points for the highest two wind speeds suggest that the drag coefficient may actually plateau at high wind speeds. Recently, [Donelan et al. \(2004\)](#) found that the drag coefficient indeed becomes independent of wind speed above $U_{10} = 33 \text{ m s}^{-1}$. Figure 1a shows the results from the model for a fetch of 10 m. For comparison, we also show the experimental drag coefficients from Kunishi and Imasoto (see [Kondo 1975](#)) and [Donelan et al. \(2004\)](#),¹ as well as the model results from KM07. At low wind speeds, both our model and the KM07 model predict a higher drag coefficient than the experimental dataset. At moderate wind speeds, our model follows the [Donelan et al. \(2004\)](#) data until roughly $U_{10} = 35 \text{ m s}^{-1}$, and the KM07 model follows the Kunishi and Imasoto data. This consistent overestimation of the drag coefficient is most likely due to an overestimation of the viscous stress, which will be discussed subsequently. At the higher wind speeds, both models show a trend toward the saturation of the drag coefficient, but neither achieves a plateau entirely as the [Donelan et al. \(2004\)](#) data suggest. Figure 1b shows the relative contributions of stress components as a function of wind speed, and the maximum fraction of separation stress is roughly 0.7 compared to 0.9 in KM07. It is difficult to compare directly the stress fractions to KM07 since the total stress used to normalize the stress components is different between the models. For example, the fraction of viscous stress would be lower at higher wind speeds, if the total stress were higher. Likewise, if the viscous stress were lower, the fraction of wave-induced and separation stresses would also be higher.

We now consider an additional modification of the viscous stress. The laboratory experiments of [Jähne and Riemer \(1990\)](#) suggest that the small gravity-capillary waves near the viscous scale are not completely smeared out of existence. Therefore, the waves, whose inner region, $l_i(k) = \hat{\delta}/k$, lies completely within the viscous sublayer, i.e. $l_i(k) < 10\nu/u_{*v}^0$, must depend on the viscous stress for growth rather than the turbulent stress that is negligible within this layer. Thus, the wave-induced stress for these waves should be subtracted from

¹ The data from [Donelan et al. \(2004\)](#) were averaged over the different methods used in their study, as suggested by Mark Donelan (2008, personal communication).

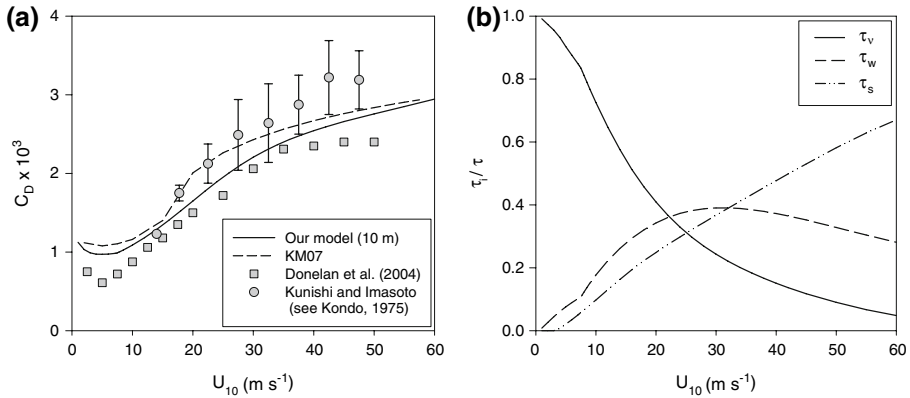


Fig. 1 **a** Drag coefficient as a function of wind speed for a 10-m fetch (solid line) along with the experimental data of Kunishi and Imasoto (circles) and Donelan et al. (2004) (squares). Model results from KM07 (dashed line) are also included. **b** Fraction of the viscous (line), wave-induced (dashed), and separation (dash-dotted) stresses as a function of wind speed for 10-m fetch

the nominal viscous stress calculated from the smooth flow limit. This subtraction is done before accounting for the air-flow separation sheltering effects. Although the value for the normalized height of the inner region, $\hat{\delta}$, is still debated, we take the conservative estimate $\hat{\delta} = 0.1$, and in conjunction with the conservative estimate for the viscous sublayer height, we find a lower bound of wave growth due to viscous stress. Therefore, the fully modified viscous stress, accounting for both air-flow separation and small wind wave growth becomes:

$$f_v = f_1 \tau_v^{-1} \left(\tau_v - \int_{k_v}^{\infty} d\tau_w \right), \tag{28}$$

where $k_v = \hat{\delta} u_{*v}^0 / 10\nu$.

When using f_1 in the model, the only mechanism for the viscous stress to depart from the smooth flow limit is the effect of air-flow separation. It is reasonable to believe that the smallest capillary-gravity waves play an important role in altering the viscous stress relative to the smooth flow limit, hence the introduction of f_v . Figure 2 plots the viscous stress produced by the model versus the total stress, along with laboratory data from Banner and Peirson (1998). For comparison, the data from Kukulka and Hara (2005), hereafter KH2005, are also shown. Note that the jaggedness of the results for both our model and KH2005 are due to the data spanning different fetches. Because of the extremely narrow wave spectra at these short fetches, we assume a constant exponent ($p = 1$) in the expression for the directionality of the wave growth rate. From Fig. 2, we can infer that viscous stress reduction caused by air-flow separation is not likely to be the only mechanism for the reduction of viscous stress relative to the smooth flow limit. In fact, our model overestimates the viscous stress when using f_1 , which is when it accounts only for the separation effects on the viscous stress. The laboratory fetches for these runs are especially small, (2.45 m, 3.10 m, and 4.35 m), so that the smallest waves arguably affect the viscous stress proportionately more than for longer fetches. Nevertheless, when accounting for both the effects due to separation and the wave growth of the smallest waves (by using f_v), the predicted viscous stress follows the experimental data of Banner and Peirson (1998) quite well. Figure 3 is the extension of Fig. 2 to higher wind speeds (i.e. total stress) for a 4.35-m fetch. At high wind speeds, both

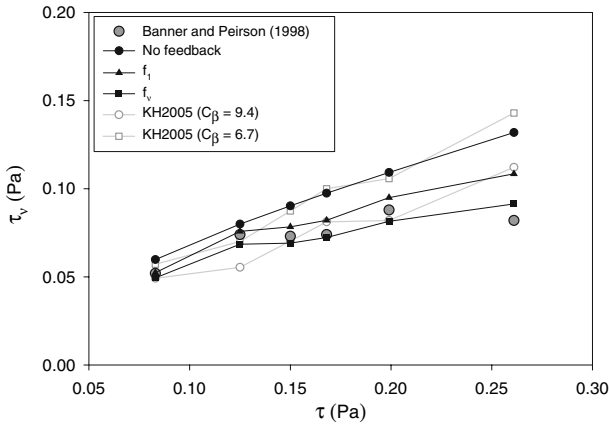


Fig. 2 Viscous stress as a function of total stress calculated with no feedback (*closed circles*), f_1 (*closed triangles*), and f_v (*closed squares*) along with the experimental data of **Banner and Peirson (1998)** (*grey circles*) and the **Kukulka and Hara (2005)** model results with sheltering and infinite wave growth constants, $c_\beta = 9.4$ (*open circles*) and $c_\beta = 6.7$ (*open squares*)

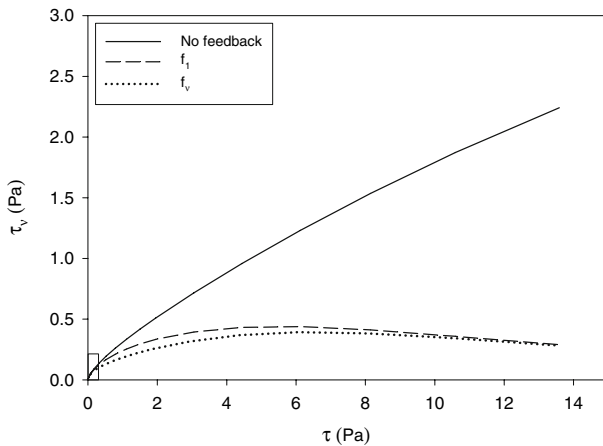


Fig. 3 Viscous stress as a function of total stress for a fetch of 4.35 m and U_{10} from 1 m s^{-1} to 55 m s^{-1} calculated with no feedback (*line*), f_1 (*dashed*), and f_v (*dotted*) with the range of experimental data from **Fig. 2** denoted by the solid box

estimates of τ_v are roughly the same, which is a consequence of more prevalent air-flow separation and of a thinner viscous layer. Because of the latter, the inner regions of few waves are encapsulated by the viscous layer at high wind speeds. In other words, the additional influence of the waves on the viscous stress is significant at either short fetches, such as laboratory conditions, or perhaps in the field under low wind speeds. Consequently, the drag coefficient, when including the effect of the smallest waves on the viscous stress, does not substantially change at the lowest and highest wind speeds, but within the wind speed range $10\text{--}25 \text{ m s}^{-1}$ it is slightly reduced from that shown in **Fig. 1**. Therefore, while this additional feedback mechanism perhaps explains the viscous stress at lower wind speeds, it does not explain the flattening drag coefficient at high wind speeds as seen in the experimental data of **Donelan et al. (2004)**.

4.2 Field Comparison

Field fetches of 1 km or more have more practical importance than the laboratory fetches discussed in the previous section. With increasing fetch, the wave field becomes more developed for each particular wind speed, which means that the short, laboratory fetches provide steeper waves and consequently more fractional area affected by air-flow separation per event. In the ocean, each separation event covers less fractional area, but because there are more events, the total sheltered area is greater. Our model predicts a drag coefficient that reaches near saturation for field fetches. Figure 4a shows our predicted drag coefficient for 10-km and 100-km fetches as well as the infinite limit. For comparison, we also show the drag coefficient of Large and Pond (1981), the data from Taylor and Yelland (2000), and the data from Powell et al. (2003) along with the KM07 model results for a 100-km fetch. For the most part, all of the data at low wind speeds are roughly constant, which is consistent with the Large and Pond (1981) estimate. At moderate wind speeds, the 10-km, 100-km and infinite fetch cases seem to follow Taylor and Yelland (2000). All of the modelled field drag coefficients nearly plateau somewhere between 30 m s^{-1} and 40 m s^{-1} , even in the infinite fetch limit. After 40 m s^{-1} , the drag coefficients for all fetches continue to increase ever so slightly. The drag coefficient follows the upper limit of the Powell et al. (2003) data up to 40 m s^{-1} but never decreases as their data suggest. This downward trend with decreasing fetch is consistent with the conclusion of Moon et al. (2004) that the observed reduction of the drag coefficients of Powell et al. (2003) could be due to an extremely limited fetch. Another possibility, though not explicitly considered here, is the potential impact of sea spray on the drag coefficient at high winds (Andreas 2004; Barenblatt et al. 2005; Makin 2005; Kudryavtsev 2006).

Figure 4b plots the fraction of the individual stress components relative to the total stress for the 100-km fetch. As with the 10-m fetch case shown in Fig. 1b, separation stress appears to play a similar role as it carries roughly the same fraction of the total stress. The maximum fraction of separation stress is roughly 0.7 compared to 0.6 in KM07. Even though KM07 maximize the downwind length of the separation bubble ($L = 1$), their model predicts a substantially greater total stress at high winds as seen in Fig. 4a. Despite a lower fraction of

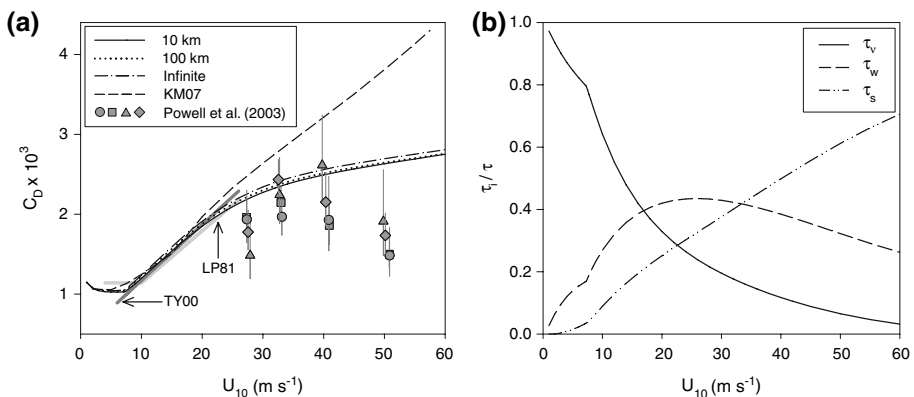
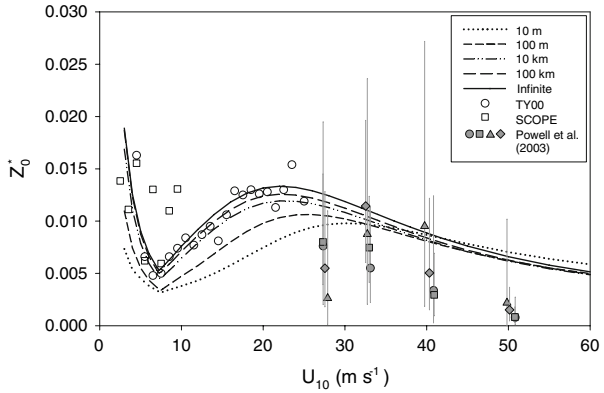


Fig. 4 **a** Drag coefficient as a function of wind speed for 10-km (solid), 100-km (dotted), and infinite (dash-dotted) fetches along with the experimental data of Large and Pond (1981) (light grey), Taylor and Yelland (2000) (dark grey) and Powell et al. (2003) (grey symbols). Model results from KM07 (dashed line) are also included. **b** Fraction of the viscous (line), wave-induced (dashed), and separation (dash-dotted) stresses as a function of wind speed for a 100-km fetch

Fig. 5 Nondimensional roughness as a function of wind speed for 10-m (*dotted*), 100-m (*short dashed*), 10-km (*dash-dot-dotted*), 100-km (*long dashed*), and infinite (*line*) fetches along with estimates from various field programs: Taylor and Yelland (2000) (*open circles*), SCOPE (*open squares*) and Powell et al. (2003) (*grey symbols*)



separation stress, the actual separation stress in KM07 is greater than that predicted by our model.

The nondimensional roughness length, or Charnock constant, can further illustrate the different effect of air-flow separation for laboratory and field fetches. Accounting for the smooth flow roughness, the nondimensional roughness due to surface gravity waves is:

$$Z_0^* = \frac{g}{u_*^2} \left(z_0 - \frac{0.11\nu}{u_{*v}} \right). \tag{29}$$

Figure 5 shows the nondimensional roughness length for several fetches as a function of wind speed. There is similar behavior for all fetches, while the peak roughness, however, shifts to higher wind speeds with decreasing fetch. At low wind speeds, the Charnock coefficient is within the estimates found from the San Clemente Ocean Probing Experiment (SCOPE; Edson and Fairall 1998) and Taylor and Yelland (2000). At high wind speeds, our results are within the Powell et al. (2003) error ranges for wind speeds up to 50 m s^{-1} . It is also interesting that the roughness for the 10-m fetch decreases less sharply at high wind speeds. Since the behaviour of field and laboratory fetches is similar, Fig. 5 suggests that the roughness length coefficient for field fetches decreases more than that for laboratory fetches at high winds. If this is indeed the case, air-flow separation effects could partially explain the relative drag coefficients of Powell et al. (2003) and Donelan et al. (2004). Nevertheless, this model also suggests that air-flow separation effects are unable to cause the reduction of the drag coefficient at high wind speeds as seen in the data of Powell et al. (2003), because a reduction in the drag coefficient implies a sharply decreasing roughness length coefficient.

4.3 Wave-age Dependence

In this section we consider the influence of the wave age on the stress components. This examination offers additional insight to that gained from looking at the dependence on wind speed and fetch. We consider a range of inverse wave ages ($\Omega \approx 0.84 - 7$) that cover the range of wind speeds and field-scale fetches considered in the previous section.

The fraction of sheltered area as a function of wind speed, shown in Fig. 6a, does not appear to depend strongly on inverse wave ages that are representative of field-scale fetches. At low wind speeds, the younger waves ($\Omega = 7$) provide less fractional sheltering, but at higher wind speeds this order reverses so that younger waves provide greater sheltering.

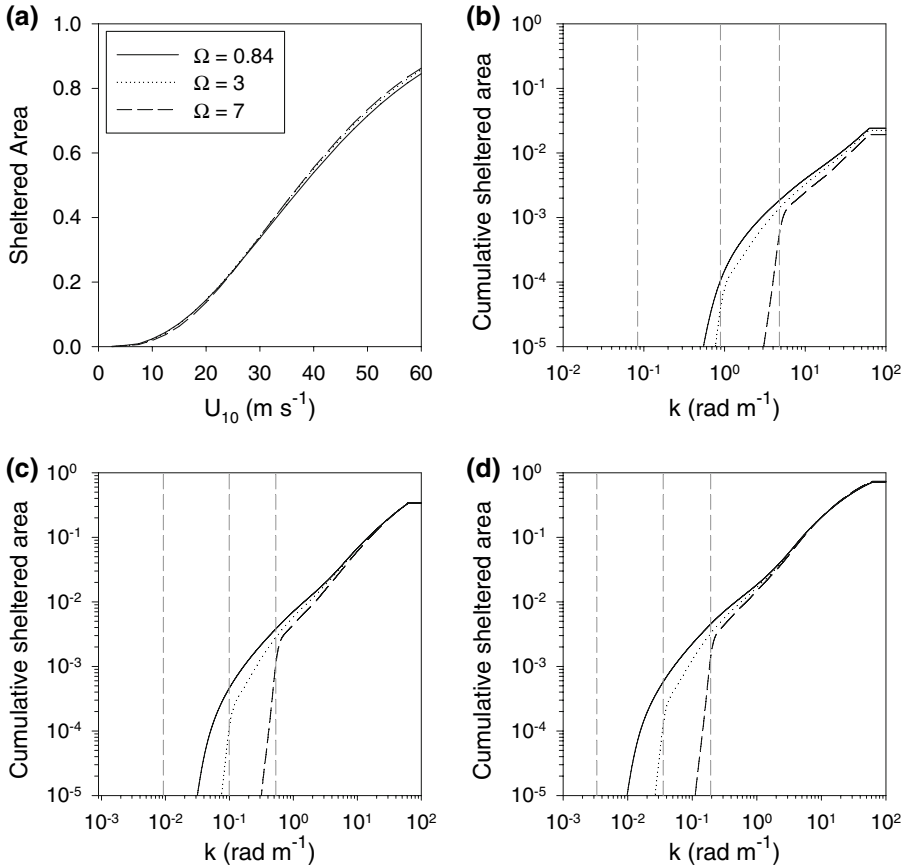


Fig. 6 a Fraction of sheltered area as a function of 10-m wind speed for inverse wave ages $\Omega = 0.84$ (line), $\Omega = 3$ (dotted) and $\Omega = 7$ (dashed) along with the cumulative fraction of sheltered area as a function of wavenumber for **b** $U_{10} = 10 m s^{-1}$, **c** $U_{10} = 30 m s^{-1}$ and **d** $U_{10} = 50 m s^{-1}$. The grey dashed lines are the wave spectral peaks for inverse wave ages $\Omega = 0.84$, $\Omega = 3$ and $\Omega = 7$ from left to right

Extremely young waves, such as those at the laboratory-scale fetches ($\Omega > 10$), provide less sheltering for all wind speeds. In fact, the sheltered area produced by extremely young waves is roughly 10% lower for wind speeds greater than $30 m s^{-1}$ when $30 < \Omega < 45$. Nevertheless, the difference between 10-km and 100-km fetches does not produce a sufficient change in wave age to alter the sheltering substantially. Figure 6b, c and d shows the cumulative sheltered area as a function of the wavenumber for wind speeds $10 m s^{-1}$, $30 m s^{-1}$ and $50 m s^{-1}$, respectively. At $10 m s^{-1}$, the dominant waves account for close to 10% of the sheltered area for the youngest wave age shown ($\Omega = 7$). For $\Omega = 3$, the dominant waves only account for a few percent of the sheltered area, while for a fully developed sea ($\Omega = 0.84$) the dominant waves do not contribute much to the sheltered area. At $30 m s^{-1}$, the dominant waves only account for a few percent of the sheltered area even at $\Omega = 7$. By $50 m s^{-1}$, this area reduces to about one percent. The predominant role of shorter waves ($k > 1$), even at high winds, is consistent with the results shown slightly differently in KM07 (their Figs. 2b, 5b).

Figure 7a and b plot the cumulative wave-induced stress and separation stress, respectively, as a function of wavenumber for a wind speed of $10 m s^{-1}$. At this wind speed, the

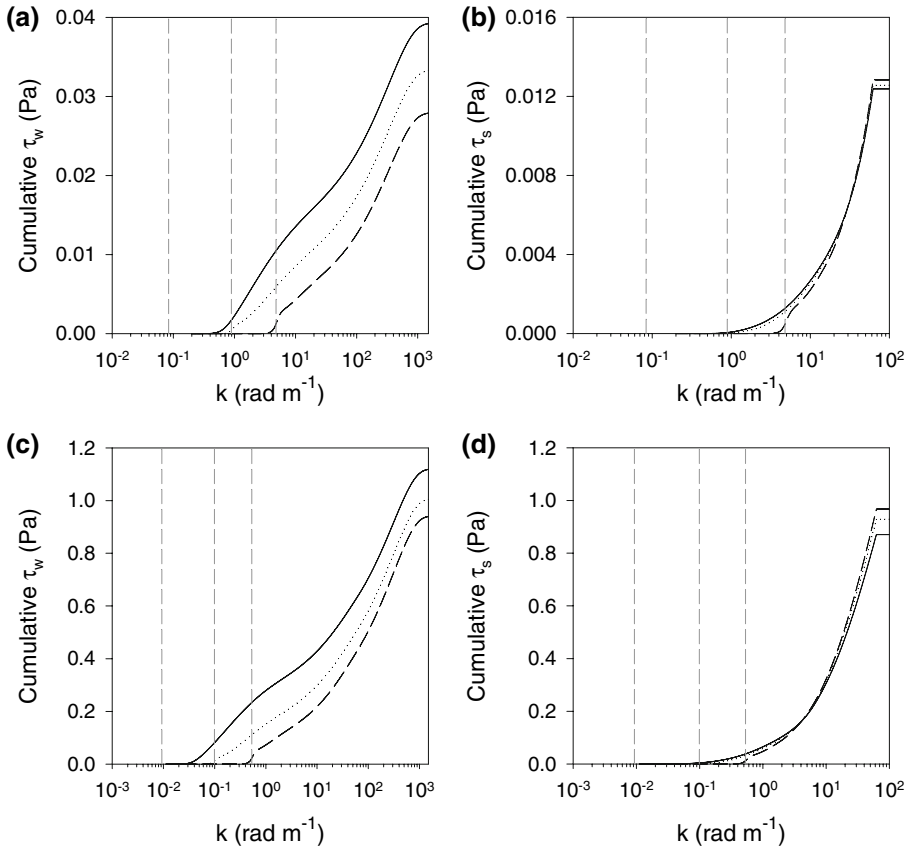


Fig. 7 (a, c) Cumulative wave-induced stress and (b, d) cumulative separation stress as a function of wavenumber for (a, b) $U_{10} = 10 \text{ m s}^{-1}$ and (c, d) $U_{10} = 30 \text{ m s}^{-1}$ with the same inverse wave age notation as Fig. 6. The grey dashed lines are the wave spectral peaks for inverse wave ages $\Omega = 0.84$, $\Omega = 3$ and $\Omega = 7$ from left to right

total wave-induced stress is roughly two to three times the total separation stress, depending on the wave age. The wave age has a greater influence on the wave-induced stress compared to the separation stress because of the relative contributions of the longer waves to both stress components. As the sea develops, the waves near the spectral peak contribute less to the wave-induced stress. Like the sheltered area, shorter waves dominate the separation stress. At this wind speed, our model predicts that waves longer than 1 m account for somewhere between 5 and 30% of the total wave-induced stress and roughly 10% of the separation stress, depending on wave age. Figure 7c and d plot the cumulative wave-induced stress and separation stress, respectively, for a wind speed of 30 m s^{-1} . At this wind speed, the total wave-induced stress is roughly the same as the total separation stress. Figure 7d clearly shows that the longer waves for the two older seas ($\Omega = 3$ and $\Omega = 0.84$) contribute roughly the same separation stress, while the shorter waves for the fully developed sea account for more separation stress. Because the magnitude of these shorter waves depend on the total stress in the model, the fully developed sea naturally contains more wave-induced stress at these shorter wavelengths. In other words, the fully developed sea produces more wave-induced

stress without sufficient, additional sheltering (as seen in Fig. 6) or reduction of the separation stress. At a wind speed of 30 m s^{-1} , our model predicts that waves longer than 1 m account for somewhere between 15 and 40% of the wave-induced stress and roughly 20–25% of the separation stress, depending on wave age. The lower bounds for these percentages are not much lower even when extremely young sea conditions are included. At laboratory-scale fetches, where these extremely young seas occur, the waves close to the spectral peak are much shorter and account for a more substantial portion of both wave-induced and separation stresses.

5 Discussion and Conclusion

Although empirical wave spectra and breaking wave statistics are extrapolated beyond known limits, the present model appears to reproduce the observed trend of the drag coefficient across different fetches as well as, if not better than, available models, which also use similar extrapolations. We note, however, that the spectral description of the wave-induced stress and separation stress (Eqs. 11, 12) rely on the assumption that the wave field can be adequately represented by linear Fourier modes. This assumption is questionable in the presence of frequent breaking at the higher wind speeds. We also note that the breaking wave statistics used here may very well underestimate actual breaking events, as they rely on equilibrium between input and dissipation, that might not be the case in growing seas, and are based on estimating the normalized dissipation b that which remains contentious to this day. This could be especially prevalent in the laboratory. Furthermore, air-flow separation may also occur without any observable wave breaking, though this remains controversial. In any event, it is likely that air-flow separation is more prevalent than its parameterization in both previous studies and this one (e.g. Veron et al. 2007).

Nonetheless, this nonlinear stress model, which includes refinements based on recent measurements, can qualitatively reproduce the observed features of the drag coefficient at low and high wind speeds. The air-flow separation effects are modelled primarily through the reduction of the viscous stress within separation zones similar to the model in KM07. These results, to the best of our knowledge, are the first that explicitly includes air-flow separation, and reproduces the saturation of the drag coefficient at high wind speeds for field-scale fetches. From this model, air-flow separation does not seem to account for the decrease in drag coefficient seen in Powell et al. (2003) and more recently in Black et al. (2007). We note, however, that the effect of sea spray may also need to be considered at higher wind speeds as recent studies have predicted a significant momentum exchange due to spray (e.g. Andreas 2004; Barenblatt et al. 2005; Makin 2005). In fact, if sea-spray generation is also a function of wave slope, its contribution to the air-sea momentum flux may in fact further reduce the predicted drag coefficient above 40 m s^{-1} and further improve the agreement between predicted and observed drag at high wind speeds (Figs. 1 and 4). This is the subject of current work and will be reported in subsequent publications. Our results indicate that air-flow separation over ocean waves and the accompanying effects and feedbacks on the multiple stress components may account for much of the observed trends. Finally, the model results suggest that air-flow separation on a range of scales eventually causes a saturation of the drag coefficient regardless of the fetch.

Acknowledgements We are grateful for the assistance of Tanos ‘Tony’ Elfouhaily in resolving the wave spectrum model and sincerely regret his untimely passing. We would also like to thank Vladimir Makin for his helpful suggestions and providing the data from KM07. We also would like to thank Mark Donelan, Mark

Powell and Tobias Kukulka for providing their data for comparison with the model. This work was supported by ONR grant (N00014-05-1-0609) to Veron.

References

- Andreas EL (2004) Spray stress revisited. *J Phys Oceanogr* 34:1429–1440
- Banner ML, Peirson WL (1998) Tangential stress beneath wind-driven air-water interfaces. *J Fluid Mech* 364:115–145
- Banner ML, Peirson WL (2007) Wave breaking onset and strength for two-dimensional deep-water wave groups. *J Fluid Mech* 585:93–115
- Barenblatt GI, Chorin AJ, Prostokishin VM (2005) A note concerning the Lighthill “sandwich model” of tropical cyclones. *Proc Natl Acad Sci USA* 102:11148–11150
- Belcher SE (1999) Wave growth by non-separated sheltering. *Eur J Mech B Fluids* 18:447–462
- Belcher SE, Hunt JCR (1993) Turbulent shear flow over slowly moving waves. *J Fluid Mech* 251:119–148
- Black PG, D’Asaro EA, Drennan WM, French JR, Niiler PP, Sanford TB, Terrill EJ, Walsh EJ, Zhang JA (2007) Air-sea exchange in hurricanes: synthesis of observations from the coupled boundary layer air-sea transfer experiment. *Bull Am Meteorol Soc* 88:354–374
- Cox CS, Munk WH (1954) Statistics of the sea surface derived from Sun glitter. *J Mar Res* 13:198–227
- Csanady GT (1985) Air-sea momentum transfer by means of short-crested wavelets. *J Phys Oceanogr* 15:1486–1501
- Donelan MA, Haus BK, Reul N, Plane WJ, Stiassnie M, Grabber HC, Brown OB, Saltzman ES (2004) On the limiting aerodynamics roughness on the ocean in very strong winds. *Geophys Res Lett* 31:L18306. doi:10.1029/2004GL019460
- Drazen D (2006) Laboratory studies of nonlinear and breaking surface waves. Dissertation, University of California, San Diego, 174 pp
- Drazen DA, Melville WK, Lenain L (2008) Inertial scaling of dissipation in unsteady breaking waves. *J Fluid Mech* 611:307–332
- Duncan JH (1981) An experimental investigation of breaking waves produced by a towed hydrofoil. *Proc R Soc Lond A* 377:331–348
- Edson JB, Fairall CW (1998) Similarity relationships in the marine atmospheric surface layer for terms in the TKE and scalar variance budgets. *J Atmos Sci* 55:2311–2328
- Elfouhaily T, Chapron B, Katsaros K, Vandemark D (1997) A unified directional spectrum for long and short wind-driven waves. *J Geophys Res* 102:15781–15796
- Garratt JR (1977) Review of drag coefficients over oceans and continents. *Mon Wea Rev* 105:915–929
- Hara T, Belcher SE (2002) Wind forcing in the equilibrium range of wind-wave spectra. *J Fluid Mech* 470:223–245
- Hara T, Bock EJ, Lyzenga D (1994) In situ measurements of capillary-gravity wave spectra using a scanning laser slope gauge and microwave radars. *J Geophys Res* 99:12593–12602
- Hare JE, Hara T, Edson JB, Wilczak JM (1997) A similarity analysis of the structure of airflow over surface waves. *J Phys Oceanogr* 27:1018–1037
- Jähne B, Riemer JS (1990) Two dimensional wave number spectra of small-scale water surface waves. *J Geophys Res* 95:11531–11546
- Janssen PAEM (1989) Wind induced stress and the drag of air flow over sea waves. *J Phys Oceanogr* 19:745–754
- Kitaigorodskii SA (1973) The physics of air-sea interaction. Israel Program for Scientific Translations, Jerusalem (English translation), 237 pp
- Kondo J (1975) Air-sea bulk transfer coefficients in diabatic conditions. *Boundary-Layer Meteorol* 9:91–112
- Kudryavtsev VN (2006) On effect of sea drops on atmospheric boundary layer. *J Geophys Res* 111:C07020. doi:10.1029/2005JC002970
- Kudryavtsev VN, Makin VK (2001) The impact of air-flow separation on the drag of the sea-surface. *Boundary-Layer Meteorol* 98:155–171
- Kudryavtsev VN, Makin VK (2007) Aerodynamic roughness of the sea surface at high winds. *Boundary-Layer Meteorol* 125:298–303
- Kukulka T, Hara T (2005) Momentum flux budget analysis of wind-driven air-water interfaces. *J Geophys Res* 110:C12020. doi:10.1029/2004JC002844
- Large WG, Pond S (1981) Open ocean momentum flux measurements in moderate to strong winds. *J Phys Oceanogr* 11:324–336

- Makin VK (2005) A note on the drag of the sea surface at hurricane winds. *Boundary-Layer Meteorol* 115:169–176
- Makin VK, Kudryavtsev VN (1999) Coupled sea surface-atmosphere model: 1. *J Geophys Res* 104:7613–7623
- Makin VK, Kudryavtsev VN (2002) Impact of dominant waves on sea drag. *Boundary-Layer Meteorol* 103:83–99
- Makin VK, Kudryavtsev VN, Mastenbroek C (1995) Drag of the sea surface. *Boundary-Layer Meteorol* 73:159–182
- Melville WK (1994) Energy dissipation by breaking waves. *J Phys Oceanogr* 24:2041–2049
- Moon IJ, Ginis I, Hara T, Belcher SE, Tolman HL (2004) Effect of surface waves on air-sea momentum exchange. Part I: effect of mature and growing seas. *J Atmos Sci* 61:2321–2333
- Phillips OM (1985) Spectral and statistical properties of the equilibrium range in wind-generated gravity waves. *J Fluid Mech* 156:505–531
- Phillips OM, Posner FL, Hansen JP (2001) High range resolution radar measurements of the speed distribution of breaking events in wind-generated ocean waves: Surface impulse and wave energy dissipation rates. *J Phys Oceanogr* 31:450–460
- Plant WJ (1982) A relationship between wind stress and wave slope. *J Geophys Res* 87:1961–1967
- Powell MD, Vickery PJ, Reinhold TA (2003) Reduced drag coefficient for high wind speeds in tropical cyclones. *Nature* 422:279–283
- Reul N (1998) Etude expérimentale de la structure de l'écoulement d'air au-dessus de vagues courtes déferlantes. Dissertation, University de la Méditerranée, Marseille, France, 334 pp
- Reul N, Branger H, Giovanangeli J-P (2008) Air flow structure over short-gravity breaking water waves. *Boundary-Layer Meteorol* 126:477–505
- Taylor PK, Yelland MJ (2000) On the apparent “imbalance” term in the turbulent kinetic energy budget. *J Atmos Ocean Tech* 17:82–89
- van Driest ER (1956) On turbulent flow near a wall. *J Aeronaut Sci* 23:1007–1011
- Veron F, Saxena G, Misra SK (2007) Measurements of the viscous tangential stress in the airflow above wind waves. *Geophys Res Lett* 34:L19603. doi:[10.1029/2007GL031242](https://doi.org/10.1029/2007GL031242)
- Wu J (1983) Sea-surface drift currents induced by wind and waves. *J Phys Oceanogr* 13:1441–1451
- Wu CH, Yao A (2004) Laboratory measurements of limiting freak waves on currents. *J Geophys Res* 109: C12002, doi:[10.1029/2004JC002612](https://doi.org/10.1029/2004JC002612)